Original Article

Processing of SiC nano-reinforced AlSi9Cu3 composites by stir mixing, ultrasonication and high pressure die casting

Guangyu Liu[*], *Mahfuz Karim, Shihao Wang, Dmitry Eskin, Brian McKay*

BCAST, Brunel University London, Uxbridge, Middlesex, UB8 3PH, United Kingdom

ARTICLE INFO

ABSTRACT

Aluminium composites have been extensively developed for automotive applications due to their high specific strength. However, particle agglomeration, high porosity content, and weak reinforcement/matrix interface bond are prone to occur in the casting process. These arise during the introduction of the reinforcement, mould filling, and solidification process, especially when the particle sizes are approaching the nanoscale and are detrimental, with respect to the mechanical properties. By applying high pressure in conjunction with high cooling rates, an improved distribution of the reinforcing particles can be expected, as the high pressure improves the filling capacity of the composite melt, in which the fluidity is generally decreased by the added heterogeneous particles. The fine grain structure obtained under the high cooling rate is also beneficial for the distribution of the reinforcing nanoparticles during solidification. In this study, SiC nano-reinforced AlSi9Cu3 composites were developed by employing an Al−Cu-SiC$_{np}$ master alloy, stir mixing, ultrasonication and HPDC technology. The findings showed a good distribution of individual SiC particles, resulting in a reduction of ~40% in the α-Al grain size and near 10% increment in the yield strength, which was attributed to grain refinement, CTE strengthening and Orowan strengthening. Compared to commercial AlSi9Cu3 HPDC alloys, the developed AlSi9Cu3-1wt% SiC$_{np}$ composite provided an improved YS of ~187 MPa and a UTS of ~350 MPa in the as-cast state and the milestone high YS and UTS of ~370 MPa and ~468 MPa under a T6 condition, respectively.

1. Introduction

A possible combination of the ductility and toughness of an aluminium matrix with the superior strength and stiffness of ceramic reinforcements has resulted in the development of aluminium-based metal matrix composites (AMMCs) for automotive and aerospace applications [1,2]. Particulate reinforced AMMCs are of significant interest because they display isotropic mechanical properties, are easier to manufacture and are often cheaper than continuous fibre reinforced AMMCs [3].

Reinforcements are typically ceramic oxide, carbide, or nitride particles, such as Al_2O_3 [4–9], TiO_2 [10], SiO_2 [11], B_4C [12], TiC [13], SiC [14,15], Si_3N_4 [16], ZrO_2 [17], and AlN [18]. Of these, SiC and Al_2O_3 particles are most commonly used. SiC particles have a higher elastic modulus and specific strength, superior wear resistance, and greater thermal conductivity over Al_2O_3 [19], making Al/SiC_p composites more popular for components that require high wear resistance and thermal conductivity, such as pistons, brake rotors, and propeller shafts [20].

The reinforcing particulates often strengthen the aluminium composites in two respects. The first is based on classical load transfer [21], in which the load is distributed between the aluminium matrix and the reinforcing particles. This mechanism is significant in the presence of high-volume reinforcements with coarse sizes. The second involves mechanisms based on micromechanics associated with the dislocation behaviour, i.e., Orowan strengthening and coefficient of thermal expansion (CTE) mismatch strengthening [22]. This phenomenon is particularly dominant in composites reinforced by fine particles (<1 μm) [23]. Specifically, the Orowan strengthening is based on the resistance provided by the small hard particles against dislocation motion. Dislocation movement proceeds if these obstacles are bypassed by bowing, reconnecting, and forming a dislocation loop around the particles, leading to high work-hardening rates with improved strength [24,25]. The strengthening effectiveness can be considerably boosted when the reinforcing particles are uniformly dispersed, and the interspacing of the particles are sufficiently small, e.g., nanoscale [26]. On the other hand, when an AMMC is cooled from the processing or solidification temperature to room temperature, volumetric strain mismatch between the monolithic matrix and reinforcing particles may occur due to differences in CTE, which will subsequently produce geometrically necessary dislocations (GND) around reinforcing particles to accommodate the CTE difference [27,28]. Similarly, during the cooling of the AMMC in the solidification process, many dislocations can be generated due to the thermal mismatch between the matrix and the reinforcing particles [29], thereby strengthening the composites. In addition, the grain refinement effect caused by the addition of (nano)particles may potentially introduce more nucleation sites and/or provide agglomerates as obstacles to grain growth during solidification. This may increase the yield strength by the grain refinement effect or due to the reduced casting defects [30–32].

It has been well established that the effectiveness of strengthening is significantly dependant on the amount, size, and distribution of the reinforcing particles [33,34]. Microscale reinforcing particles often improve the strength but simultaneously decrease the ductility and toughness, resulting in a trade-off between strength and ductility, while the ductility and toughness of AMMCs can be significantly improved with a concurrent increase in strength by reducing the particle size to nanoscale. On the other hand, when the particle size is reduced to nanoscale, particle agglomeration/clustering, high porosity content, and a weak particle/matrix interface bond usually occur in the AMMCs casting, arising from the stirring, mould filling, and solidification [35–37]. These imperfections are detrimental to the mechanical properties [38]. For example, the clusters can act as cracks or de-cohesion nucleation sites, or both, at stresses lower than the matrix yield strength, causing the AMMCs to fail at unpredictable low-stress levels [39,40]. More importantly, due to poor wetting of the nanoparticles by the molten metal and the formation of clusters of nanoparticles in the melt from the attractive van der Waals forces, it is sometimes not feasible to uniformly disperse the nanoparticles in the molten matrix during the traditional casting process.

Stir casting combined with ultrasonic processing has been considered as a promising method for a suitable dispersion of nanoparticles in the molten matrix [41]. During ultrasonic treatment, acoustic waves generate alternating tensile–compression stress in the molten metal, leading to the formation of tiny cavities. During the expansion cycles, the cavities grow whereas during the compression cycles they collapse and produce transient (in the order of microseconds) micro "hot spots", where extremely high temperatures (5000 °C) and pressures (~1000 atm) are generated [42]. This process is called "acoustic cavitation" and can generate high-density shock waves to break the agglomerates/clusters and disperse them under acoustic streaming [43,44]. Furthermore, the local transient high temperature and pressure could significantly improve the wettability of particles by removing or desorbing the gases from the surface of the particles and decreasing the surface energy of nanoparticles in the liquid phase. At a very high local temperature (5000 °C), the surface tension of liquid with vapour is significantly decreased, which further enhances the wettability of the nanoparticles [23,45].

High-pressure die casting has been deemed a cost-effective and productive manufacturing technique for the mass production of aluminium castings with a complex near-net-shape [46]. It is especially suitable for components requiring high dimensional accuracy and no post-machining processing. These characteristics make it even more ideal for producing AMMCs, achieving a near-net-shape that will decrease post-machining, given the poor machinability of the composites [47]. Also, the high pressure applied in HPDC improves the filling capacity of the molten composites, in which the fluidity is generally decreased due to the addition of particles. Meanwhile, the fine grain structure is beneficial to the distribution of the reinforcing nanoparticles during solidification. Li et al. [48] reported that carbon nanotubes (CNTs) could be dispersed by high turbulent flow in the cavity through HPDC, by locating pre-dispersed CNTs at the entrance of the die cavity to manufacture Al/CNTs composites successfully. Hu et al. [49] suggested the improved particle distribution, reduced porosity, and good bonding at the matrix/particle interface, observed in HPDC Al/SiC_p composites (100 μm) showed a significant improvement in properties compared to samples produced by gravity casting.

The current study was aimed at manufacturing LM24 (AlSi9Cu3)-based SiC_{np} reinforced nanocomposites with good SiC nanoparticle dispersion and improved mechanical properties, by combining the advantages of stir mixing, ultrasonic processing and HPDC technology. Notably, instead of applying loose nanoparticles, an Al–15Cu-10SiC_{np} master alloy was employed as the nanoparticle source, in an attempt to improve the introduction and dispersion of the SiC particles. The distribution and effects of SiC nanoparticles on the resultant microstructure and mechanical properties were thoroughly investigated.
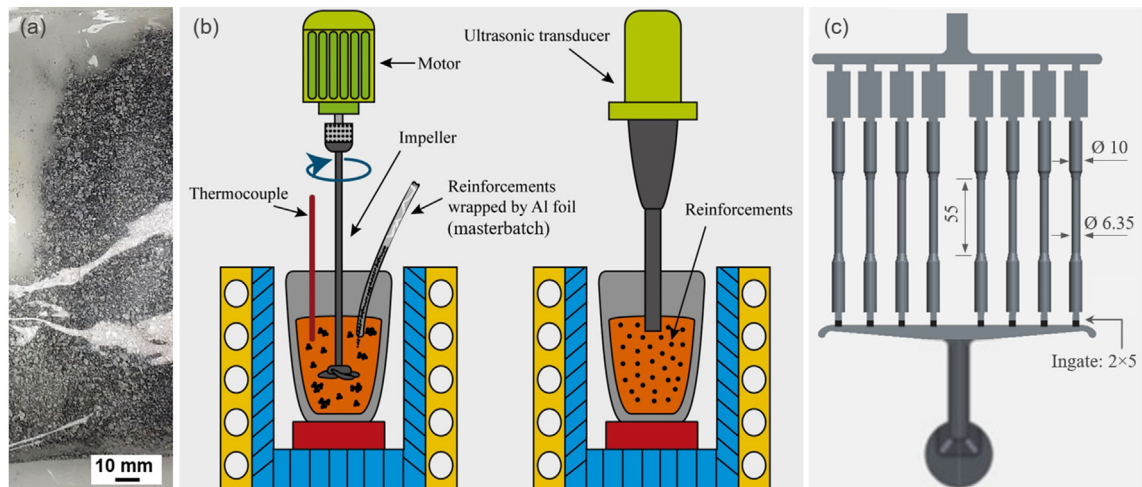
Fig. 1 − **Photos and schematics showing (a) the Al−15Cu-10SiC$_{np}$ master alloy in the form of small shots: 100−2000 μm, (b) the stir mixing process assisted by the ultrasonic treatment, (c) the geometry of the HPDC casting producing eight tensile specimens with the dimensions given in mm.**

2. Experimental

2.1. Sample preparation

Commercially pure Cu, Al−50Si, and AlSi8Cu3 ingots (supplied by Norton Aluminium Ltd., UK) were used as the raw materials to produce the baseline and composite melt. An Al-15 wt % Cu-10 wt% SiC$_{np}$ master alloy in the form of fine shots (200−2000 μm), as shown in Fig. 1a, was added to the melt to prepare the composites. The SiC particles were nanoscale (<100 nm) in size. The Al−15Cu-10SiC$_{np}$ master alloy was produced via high energy ball milling (HEBM) and supplied by MBN Nanomaterialia (Italy). The chemical compositions of the baseline alloy and the composite, measured by optical emission spectroscopy (OES, Foundry Master), are shown in Table 1.

Fig. 1b shows a schematic of the experimental setup for making the composite using the ultrasound-assisted solidification technique, which consisted of an electric resistance furnace, impeller-rotor unit, and ultrasonic unit. In total, ~3 kg of the LM24 ingots and Al−50Si alloys were placed in a clay-graphite crucible and melted in an electrical resistance furnace (Carbolite) at 750 °C. After the melt was homogenised for approximately 2 h, preheated (at 300 °C) Al−15Cu-10SiC$_{np}$ master powder wrapped in Al foil were fed into the melt at the side of the vortex created by a four-blade titanium impeller rotating in a clockwise direction. This achieved pre-mixing and thus the preliminary introduction of nanoparticles into the melt. The impeller was coated with boron nitride to prevent any reaction with the molten aluminium. In the stir

mixing process, nominal ~1 wt% SiC nanoparticles were successfully introduced into the melt, producing the composite melt, with the melt temperature decreasing in the process from 750 °C to 680 °C over a 10-min period. Then, the pre-mixed composite melt was reheated up to 750 °C before ultrasonically processing. A 17.5 kHz, 30-μm (peak-to-peak) ultrasonic wave was transmitted by a 19 mm diameter niobium probe into the melt for 15 min to achieve further dispersion of the nanoparticles. The ultrasound was generated by a 5 kW ultrasonic generator coupled to a 5 kW water-cooled magnetostrictive transducer operating at a 3.5 kW power. Post ultrasonic processing, the melt temperature dropped to 700 °C. The composite melt was then held for 1 min, before being manually poured into the shot sleeve to produce the HPDC casting. 8 tensile samples (Fig. 1c) were obtained, 6.35 mm in diameter using a Frech 4500 kN locking force cold chamber HPDC machine. The pouring temperature of the melt, die temperature, and shot sleeve temperature were 700 ± 5 °C, 200 ± 5 °C and 180 ± 5 °C, respectively.

The baseline alloy was produced using the same process except that an Al−Cu master alloy was added instead of the Al−Cu-SiC$_{np}$. No degassing was performed in all cases. The HPDC casting bars were heat-treated by applying solution treatment at 490 °C for 0.5 h, followed by an immediate quench in cold water; subsequently, the samples were artificially aged at 150 °C for 16 h [50].

2.2. Mechanical properties

Vickers hardness tests were conducted on the cross-section of the casting bars' gauge section by using a Wilson 432SVA

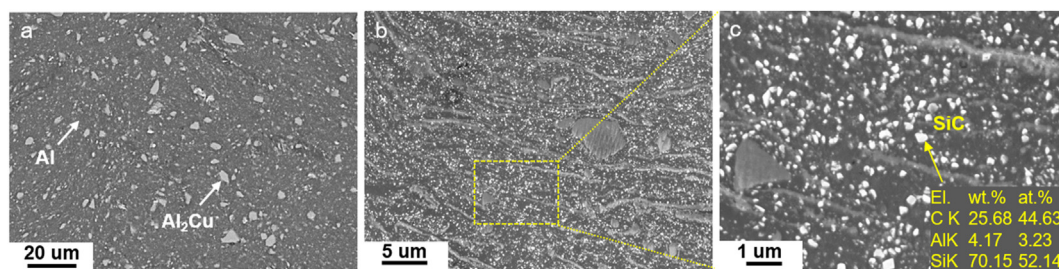| Table 1 − Chemical compositions in wt% of the baseline alloy and the LM24/SiC$_{np}$ composite.									
Materials	Al	Si	Cu	Fe	Mn	Mg	Ti	Zn	Ni	Others
Baseline	Bal	8.89	3.82	1.13	0.31	0.11	0.09	1.59	0.04	<0.001
LM24/SiC$_{np}$	Bal	9.12	3.91	1.29	0.29	0.10	0.09	1.50	0.04	<0.001

Fig. 2 – (a) BSE-SEM and (b, c) In-lens SEM micrographs showing the Al$_2$Cu intermetallic phase and SiC nanoparticles in an Al–15Cu-10SiC$_{np}$ master alloy.

digital auto-turret macro-Vickers Hardness Tester. A 10 N load and a dwell time of 10 s were applied for the hardness testing. Six indentations across the gauge section of each specimen were conducted, obtaining the mean hardness of the sample. Eight specimens were tested. Tensile testing was performed on an Instron 5500 Universal electromechanical testing system at ambient temperature. A gauge length of 50 mm and a gauge diameter of 6.35 mm were applied. The ramping rate was 1 mm/min, and a 50 mm extensometer was used to record tensile data. Each data point reported with the corresponding standard error was based on the mechanical properties attained from 15 samples.

2.3. Microstructural characterisation

The metallurgical microstructural examination was conducted on the cross-section of the cast bars at the gauge positions. The fractured tensile bars were also examined on the longitudinal cross-sections. The surface to be examined was ground using SiC abrasive papers and then polished using silica suspension (OPS, 0.05 μm water-based SiO$_2$ suspension). Quantitative analysis of the microstructure was performed using AxioVision Rel. 4.8 software integrated into a Zeiss optical microscope which was used for acquiring optical micrographs. Detailed information on intermetallic phases, reinforcing nanoparticles was obtained using a Zeiss Supra 35 field-emission scanning electron microscope (FESEM) equipped with an energy-dispersive X-ray spectroscope (EDS). The grain size was examined by using the electron back-scattered diffraction (EBSD) technique. Nano-scaled precipitates and nanoparticles were examined using 200 KeV high-resolution transmission electron microscopy, JEOL 2100F (JEOL Ltd.). The TEM samples were cut from LM24 and LM24/SiC$_{np}$ specimens and ground to a thickness of <100 μm. 3 mm diameter samples were subsequently punched and further reduced to electron transparency using a Gatan precision ion polishing system (PIPS) operating at 5.0 kV with an incident angle of 3–5°.

3. Results

3.1. Microstructure of an Al–15Cu-10SiC$_{np}$ master alloy

Fig. 2 presents SEM micrographs showing an intermetallic phase and SiC nanoparticles in the microstructure of an Al–15Cu-10SiC$_{np}$ master alloy. The microstructure mainly comprised the Al phase (dark) and fine Al$_2$Cu phase (grey, 3–8 μm) under low magnification, as shown in Fig. 2a. From Fig. 2b, it was observed that a large number of fine particles (white) were homogeneously distributed in the matrix. With closer inspection of the microstructure (Fig. 2c), these particles displayed irregular shapes with a size <100 nm. These were identified as the SiC nanoparticles, as indicated by the EDS results (Fig. 2c inset). This indicated that the SiC nanoparticles were uniformly distributed in the Al–15Cu-10SiC$_{np}$ master alloy, which was expected to improve the distribution of the particles in the melt during the stir mixing process.

3.2. Microstructure of the LM24 alloy and LM24/SiC$_{np}$ composite

3.2.1. α-Al grain size

Fig. 3 shows the optical microstructures including the primary α-Al and Al–Si eutectic phases, intermetallic compounds, and the porosity in the LM24 alloy and LM24/SiC$_{np}$ composite under the as-cast condition. It was observed that the primary α-Al phase exhibited two forms, i.e., coarse Al(α$_1$) grains nucleated in the shot sleeve with low cooling rates and fine Al(α$_2$) grains formed in the die cavity at high cooling rates. For the LM24 baseline alloy, some coarse Al(α$_1$) grains were found in the form of dendrites with a size of 50–100 μm, as indicated in Fig. 3a, while the coarse Al(α$_1$) grains observed in the LM24/SiC$_{np}$ exhibited a less dendritic morphology with smaller sizes of 30–50 μm, as indicated in Fig. 3b. The morphology of the fine Al(α$_2$) grains in both samples showed equiaxial grains < ~10 μm in size. A lower proportion of the coarse Al(α$_1$) grains were present in the LM24/SiC$_{np}$ composite compared to that of the LM24 alloy, indicating that the addition of SiC nanoparticles, to some extent, benefits refinement of the primary Al(α$_1$) phase. Other readily perceived constituents were the intermetallic compounds, including the well-established Fe-bearing and Cu-bearing intermetallic phases that will be discussed further. Pores are the common defects observed in the HPDC process, with both samples revealing some porosity. However, a higher proportion was found in the LM24/SiC$_{np}$ composite, which was attributed to the entrapment of the air during the process of stir mixing.

Fig. 4 shows the EBSD grain maps and the grain size distribution in the as-cast LM24 alloy and LM24/SiC$_{np}$ composite. The grain tolerance angle is set to 15° to distinguish the neighbouring grains (Fig. 4a and b). The Al grain size in the LM24 baseline alloy and LM24/SiC$_{np}$ composite were measured
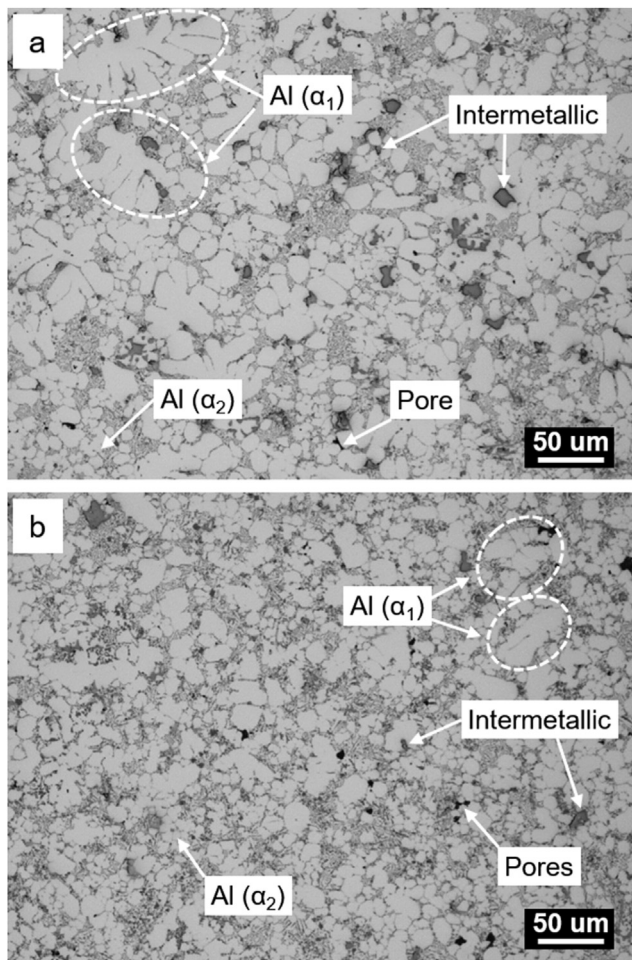
Fig. 3 – Optical micrographs showing the size and morphology of the primary α-Al phase, intermetallic compounds, and porosities in (a) the LM24 alloy and (b) the LM24/SiC$_{np}$ composite under as-cast conditions.

to be 24 ± 6 μm and 15 ± 5 μm, as shown in Fig. 4c and d, respectively, indicating a significant grain refinement (decreased by ~40%) due to the addition of SiC nanoparticles.

3.2.2. Intermetallic phases

Fig. 5 shows the size and morphology of the Fe-bearing and Cu-bearing intermetallic phases and eutectic Si particles in the as-cast and heat-treated LM24 alloys. A blocky Al$_2$Cu phase, a needle-like β-Al$_5$FeSi phase, ~10 μm in size, and a coarse polygon-shaped α-Fe$_1$ (Al$_{15}$(Fe, Mn)$_3$Si$_2$) phase, 5–10 μm in size, were readily observed in the as-cast LM24 alloy (Fig. 5a). In addition to the coarse α-Fe$_1$ phase, other fine α-Fe$_2$ particles displaying an equiaxial shape, 0.5–1 μm in size, were present, as highlighted by the white dashed circle. The corresponding chemical compositions of the individual Fe-bearing and Cu-bearing intermetallic phases highlighted by S1, S2, and S3 were analysed by EDS, as shown in Fig. 6. It has been suggested that two types of Fe-bearing intermetallic phase can form during the different stages of solidification for LM24 alloys [[51]]. The coarse Fe-bearing intermetallic phase forms in the shot sleeve, usually displaying a polyhedral or

block-shaped morphology, while the pro-eutectic Fe-bearing intermetallic phase is often nucleated and solidified in the die cavity, exhibiting polyhedral and/or hexagonal morphology with fine size. From Fig. 5, the observed coarse primary α-Fe$_1$ intermetallic phase exhibiting the polyhedral or block morphology should be the first Fe phase formed in the shot sleeve, and the fine α-Fe$_2$ intermetallic phase should be the second primary Fe phase formed in the die cavity under a higher cooling rate. It is noted that the fine α-Fe$_2$ phase showed a lower ratio of (Fe, Mn) to Si than the primary coarse α-Fe$_1$ phase, as indicated by the EDS results (Fig. 6a and b), revealing a lower level of Fe and Mn in the α-Fe$_2$ phase. This is consistent with the fact that at the late stage of solidification, fewer Fe and Mn atoms are available for the formation of the pro-eutectic α-Fe$_2$ phase, due to their consumption by the α-Fe$_1$ phase. It is also suggested that the quaternary α-Fe phase has a considerably wide homogeneity range. Therefore, its composition alters depending on the local melt compositions at a particular stage of solidification [52].

An acicular networked fibrous Si eutectic phase can be observed in the as-cast LM24 alloy, as indicated by the yellow circle in Fig. 5b. After T6 heat treatment, the spatial networked Si phase was fragmented and spheroidised. This led to the redistribution of fine and equiaxed eutectic Si particles, as shown in the region highlighted by the dotted circle Fig. 5c. Similarly, the previously blocky Al$_2$Cu network, to some extent, was broken into fine fragments (Fig. 5d) due to the partial dissolution into the Al matrix during heat treatment. The Fe-bearing particles showed no significant change due to the relatively low temperature and short time of the heat treatment.

Fig. 7 presents the SEM micrographs showing the distribution of SiC nanoparticles in the microstructure of LM24/SiC$_{np}$ composite under the condition of as-cast and T6 heat treatment. Overall, loose SiC clusters were found homogeneously distributed in the matrix, as indicated in the region highlighted by the white-dashed circles in Fig. 7a and d. These SiC clusters were dispersed mainly in the interdendritic and Al–Si eutectic regions. It is clear from Fig. 7b and e that the Al–Si eutectic region was enriched with loose SiC clusters, eutectic Si phase, and fine pro-eutectic α-Fe$_2$ particles. From high-magnification micrographs, it is found that a small amount of individual SiC nanoparticles can be agglomerated to form clusters in the vicinity of Fe-bearing or eutectic Si particles. It should be noted that no significant morphological change of the SiC particles was found after the heat treatment, which was due to the relatively low-temperature treatment. On the other hand, similar to the LM24 baseline alloys, in the LM24/SiC$_{np}$ composites, the Al$_2$Cu phase in the form of networking was segmented into fine fragments, while the Fe-bearing particles showed a marginal change after heat treatment.

3.2.3. Precipitates

Fig. 8 shows bright-field (BF) TEM images and the corresponding selected area diffraction patterns (SADPs) of the LM24 baseline alloys under as-cast and T6 heat treatment states. As viewed along <001>$_{Al}$ direction in the BF TEM image (Fig. 8a), the as-cast alloy showed a clean matrix without precipitates, which was further evidenced by the absence of any extra reflections other than reflections from the Al matrix
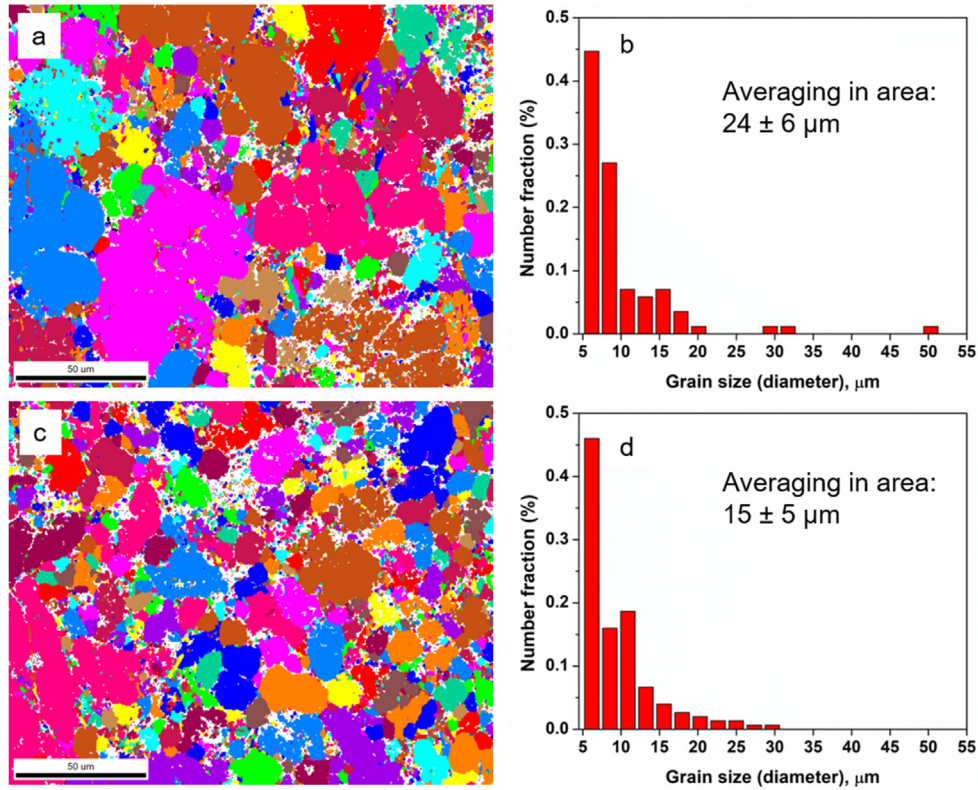
Fig. 4 − **The EBSD grain map and grain size distribution diagram obtained from the microstructure of (a, b) the LM24 alloy and (c, d) the LM24/SiC$_{np}$ composite under as-cast condition. Grain Tolerance Angle: 15.**
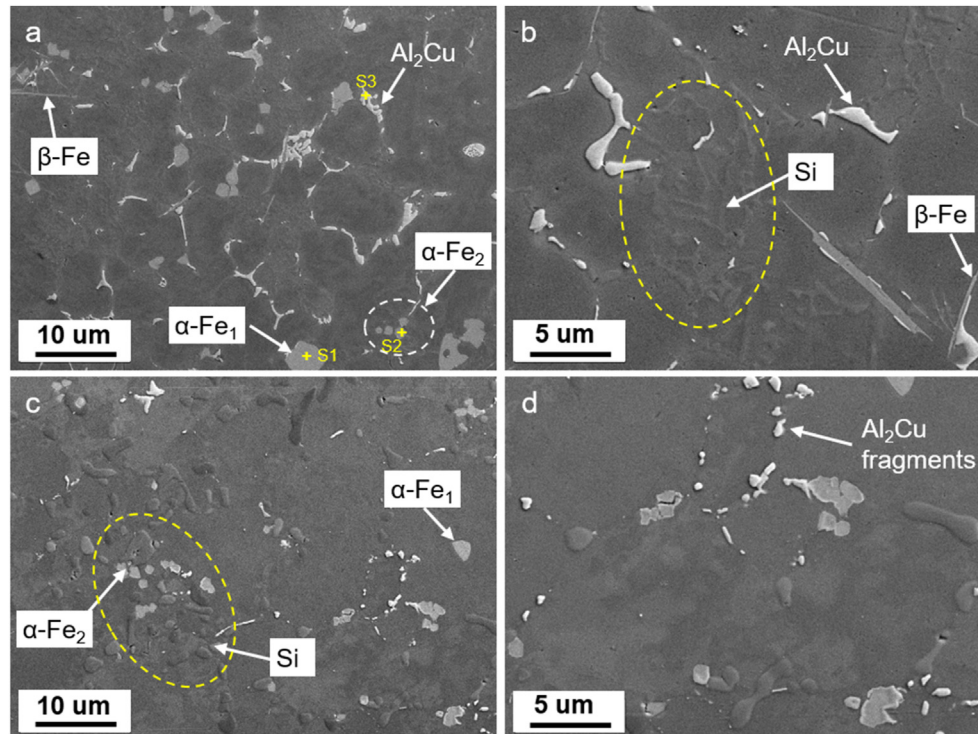

Fig. 5 − **SE−SEM micrographs showing eutectic Si phase, Fe-bearing and Cu-bearing intermetallic compounds in the LM24 alloys under (a, b) as-cast and (c, d) T6 heat treatment processing conditions.**
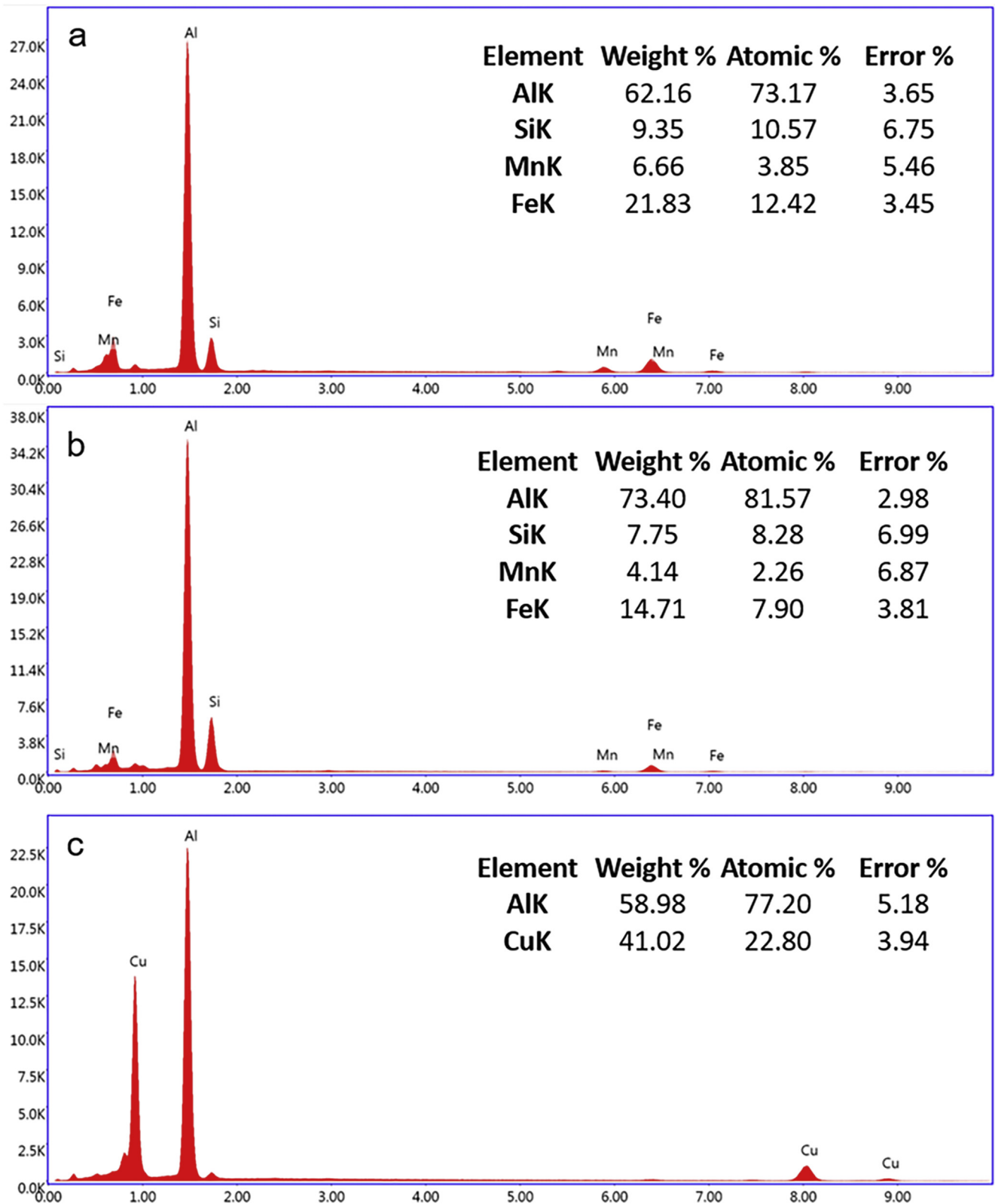
Fig. 6 − EDS spectra and analysis of the Fe-bearing and Cu-bearing intermetallic phases corresponding to points in Fig. 5: (a) S1, (b) S2, and (c) S3.
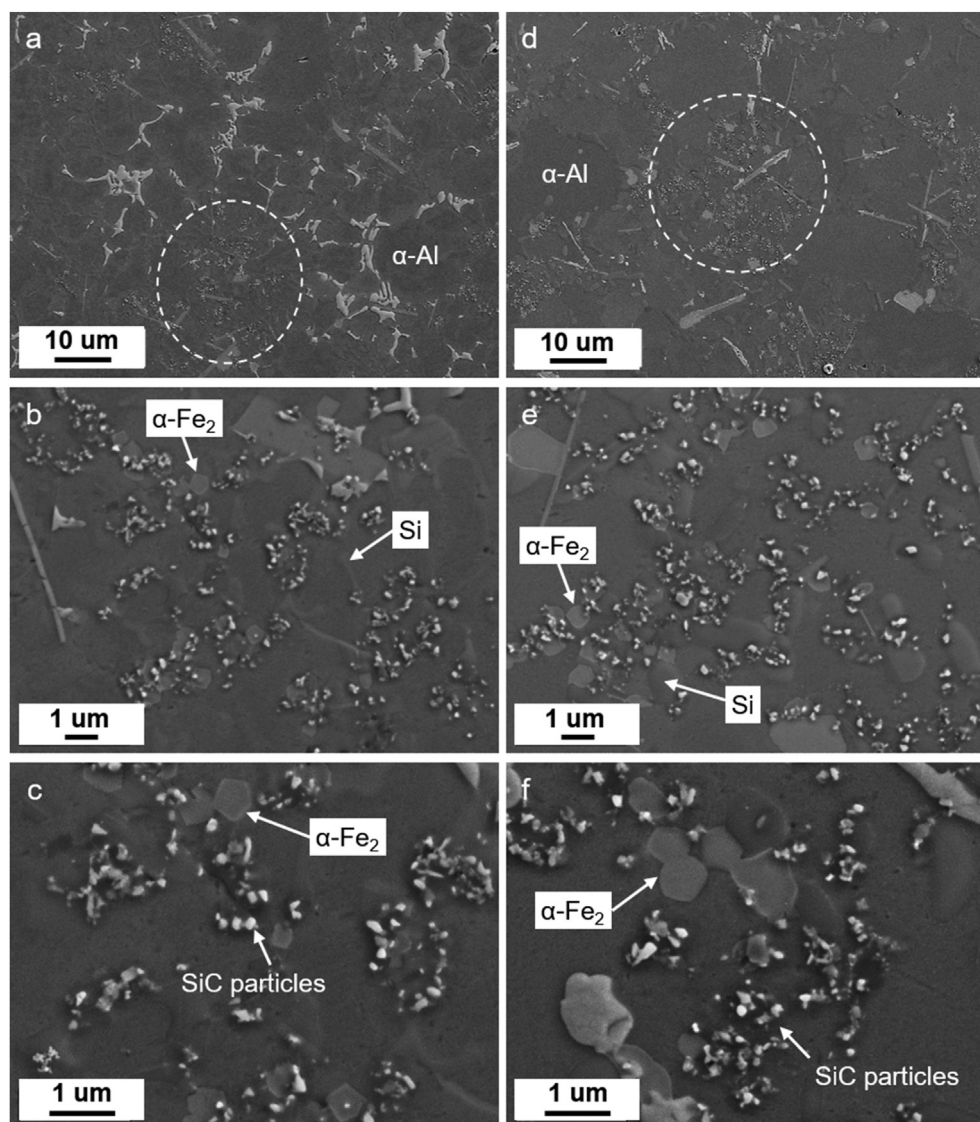
Fig. 7 — SE–SEM micrographs showing the SiC nanoparticles, eutectic Si phase, Fe-rich and Cu-rich intermetallic phases in the (a, b, c) as-cast and (d, e, f) T6 LM24/SiC$_{np}$ composites.

in the corresponding SADPs (inset in Fig. 8a). Fig. 8b shows a number of dislocations and dislocation tangles in the vicinity of the boundary between the intermetallic phase and Al matrix. In the region away from the boundary, the dislocations occur less frequently. This could be due to the large difference in the coefficient of thermal expansion (CTE) between the Al matrix and the hard and brittle intermetallic phases that causes differential strain at the intermetallic phase/matrix interface during fast cooling, with plastic relaxation leading to the generation of dislocations.

On the other hand, the application of T6 heat treatment to the as-cast alloy leads to the formation of many plate- and needle-like precipitates, as shown in Fig. 8c along the <001>$_{Al}$ direction. Faint reflections and streaks from the precipitates were seen in the SADPs along <100>Al. Considering the β″ and θ′ phase, these precipitates could be distinguished as lying or edge-on β″ phase along the <001>$_{Al}$ zone axis and lamellar θ′ phase [53,54]. So, both β″ and θ′ precipitates were, as expected,

presented in the T6 LM24 baseline alloy. Fine Si dispersoids were observed in the interior aluminium grain, as indicated in Fig. 8d. These Si dispersoids displayed a round-edge shape and possessed sizes in the range of ~50–200 nm, which will be beneficial to the enhancement of strength by impeding dislocation movements when subjected to external stress.

Fig. 9 shows bright-field (BF) and dark-field (DF) TEM images and the corresponding SADP of the LM24/SiC$_{np}$ composites after T6 heat treatment. Similar to the LM24 baseline alloy, a large number of needle-like β″ and lamellar θ′ precipitates appeared, as shown in Fig. 9a and b. Fig. 9c and d are the DF TEM images using the reflections highlighted by 'c' and 'd', showing the θ′ phase lying in the (020) and (200)Al faces, exhibiting a size less than ~50 nm in length and ~2 nm in width. The unit cell structure of the lamellar θ′ phase was analysed by the HRTEM image, and the corresponding fast Fourier transformation (FFT) is shown in Fig. 10. With the Al matrix as reference for the measurement, the precipitate
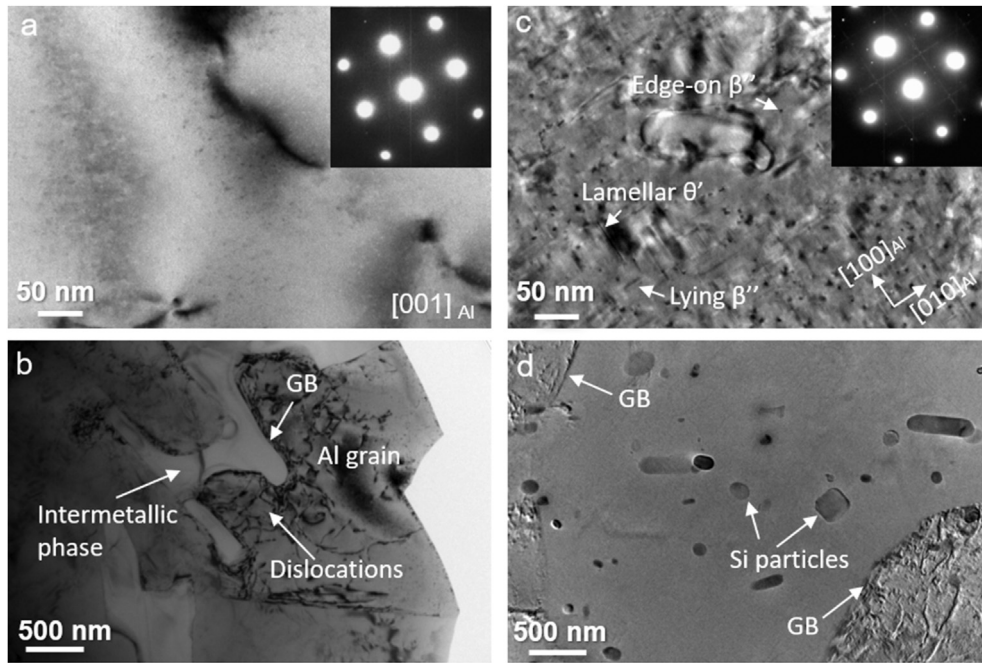
Fig. 8 − Bright-field TEM images and corresponding SADPs of the LM24 alloys under (a, b) as-cast and (c, d) T6 states.

possesses lattice parameters of a = 0.40 nm and c = 0.58 nm, and an orientation relationship with Al matrix, $(200)_{\theta'}$ ∥ $(200)_{Al}$, $[010]_{\theta'}$ ∥ $[010]_{Al}$. The structure and orientation relationship of the θ' phase is identical to that documented in previous literature [55]. As such, the predominant precipitates in the present LM24/SiC$_{np}$ composites were also β'' and θ' phases.

3.3. Hardness of the LM24 alloy and LM24/SiC$_{np}$ composite

Fig. 11 shows the Vickers hardness of the LM24 alloy and LM24/SiC$_{np}$ composite under an as-cast and T6 heat treatment conditions. The measurements were taken across the centre of the cross-section of the sample from one edge to another. In
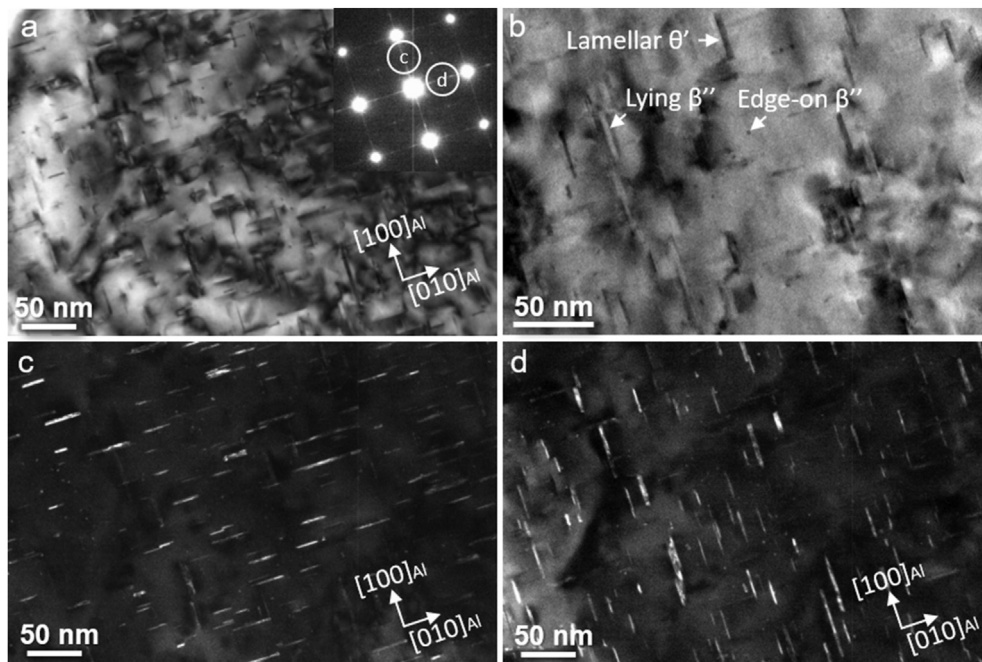

Fig. 9 − (a, b) TEM bright-field images and a corresponding SADP (inset in (a)) and the (c, d) dark-field images of the LM24/SiC$_{np}$ composites after the T6 heat treatment.
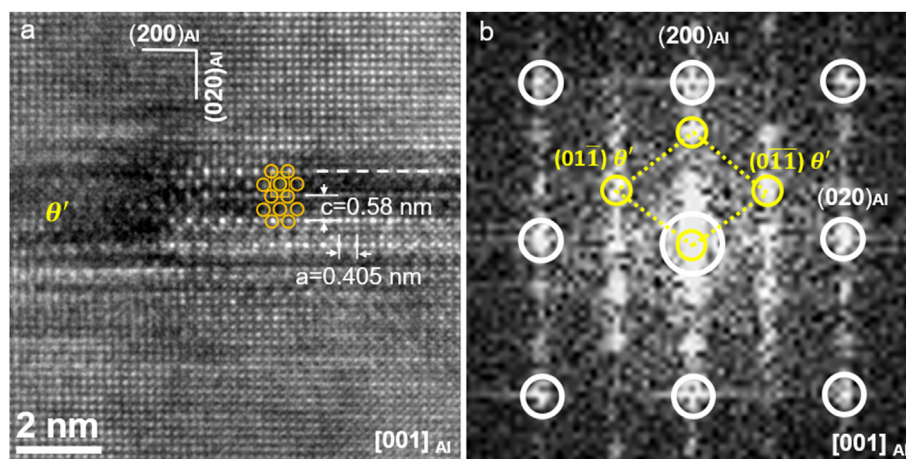
Fig. 10 – (a) High-resolution TEM images and corresponding (b) FFT images, showing the θ′ phase, in the LM24/SiC$_{np}$ composites, along the <001>$_{Al}$ axis after a T6 heat treatment.

all cases, the hardness exhibited an inhomogeneous distribution from the edge to the centre, showing higher values close to the edge. The variation in the hardness originated from the inhomogeneous microstructure across the cross-section. The region near the edge of the casting experienced a higher solidification rate, leading to a finer microstructure and fewer pores, which resulted in higher hardness. Compared with the LM24 baseline alloy, the measured hardness increased consistently for the identical positions in the LM24/SiC$_{np}$ composite, indicating some strengthening effect of the SiC particles. For the as-cast LM24, the hardness value ranged from HV94 to HV110, with an average of HV103 ± 2, while this increased to HV98-HV125 (resulting in an average value of HV111 ± 4, i.e. an increase of ~8%) for the LM24/SiC$_{np}$. After T6 heat treatment, the hardness for both samples experienced a significant increase (HV132−HV161 for LM24, and HV140−HV171for LM24/SiC$_{np}$), with the average values reaching HV152 ± 5 (an increase of ~48%) and HV160 ± 5 (an increase of~44%), respectively, compared to the as-cast conditions. The significant increase in the hardness after the T6 heat treatment was ascribed to the precipitate strengthening effect, as shown in Figs. 8−10.

3.4. Tensile properties of the LM24 alloy and LM24/SiC$_{np}$ composite

Fig. 12a shows the tensile stress−strain curves for the LM24 and LM24/SiC$_{np}$ samples under as-cast and T6 heat treatment conditions. The addition of SiC nanoparticles led to an increase in strength and a slight decrease in ductility. This was in line with the variation in hardness. The corresponding detailed tensile results are summarised in Fig. 12b. The yield strength (YS) of the as-cast LM24 was 173 ± 1 MPa, which was increased by ~8%−187 ± 1 MPa with the addition of SiC nanoparticles. At the same time, the ultimate tensile strength (UTS) was increased from 333 ± 2 MPa to 350 ± 2 MPa (an increase of 5%). The respective elongation was 3.6 ± 0.1% and 3.3 ± 0.1%, indicating a slight decrease after adding the SiC nanoparticles, which is likely to be attributed to the increased porosity introduced in the stir mixing process. After T6 heat

treatment, the YS and UTS experienced considerable increases but at a slight expense of elongation. The YS values for LM24 and the LM24/SiC$_{np}$ composite were doubled in comparison with the as-cast, reaching up to 372 ± 1 MPa and 370 ± 1 MPa, respectively. With respect to UTS, the LM24 and LM24/SiC$_{np}$ composite delivered significantly higher values of 463 ± 6 MPa and 468 ± 4 MPa, respectively. It is noted that after T6 treatment, the composites did not show noticeable improvements in the strength (YS or UTS) in comparison with the base alloy, which may be because the effect of the SiC particles was overshadowed by the precipitates.

3.5. Fractography

Fig. 13 shows the fracture microstructure of the longitudinal cross-section of the as-cast LM24 alloy subjected to the tensile
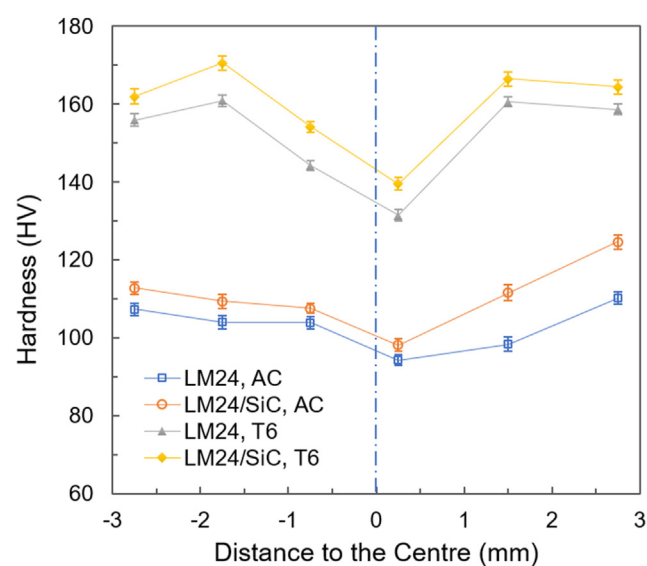

Fig. 11 – Hardness variation with the change in distance from the centre to the edge of the cross-section of the LM24 baseline alloy and LM24/SiC$_{np}$ composites in the as-cast (AC) and T6 conditions.
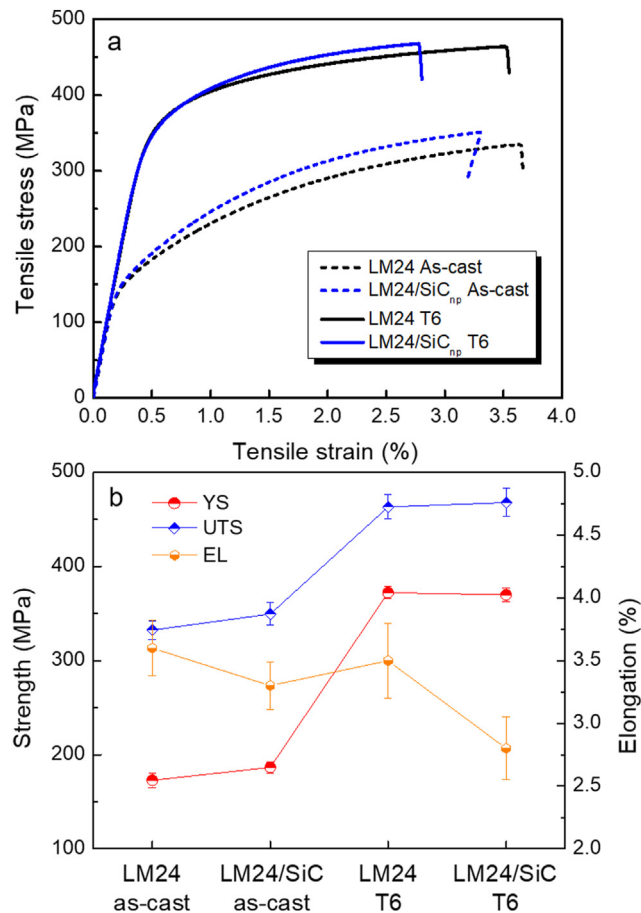
Fig. 12 − (a) Tensile stress−strain curves for the LM24 baseline alloy and LM24/SiC$_{np}$ composite under as-cast and T6 heat treatment conditions, with the tensile properties shown in (b).

Fig. 13 − SE−SEM micrographs showing the crack structure on the longitudinal cross-section of as-cast LM24 alloys subjected to the tensile test.

test. The debonding/detachment of the α-Fe intermetallic phase (both α-Fe$_1$ and α-Fe$_2$) to the adjacent Al can be observed, as indicated in Fig. 13a. Also, a crack along the β-Fe/Al interface was evident, which was in the region containing a cluster of Fe-bearing intermetallic phases. Similar debonding behaviour between the Al$_2$Cu intermetallic phase and Al matrix can be seen in Fig. 14b, as indicated by the white-dashed ellipses. In addition, cracked, brittle Si particles were visible. The interfaces between the intermetallic phases and the Al matrix are prone to debonding under external stress, making them vulnerable sites for crack initiation and subsequent propagation under further stress. The small cracks propagate and connect, leading to the final fracture of the material.

Fig. 14 shows the fracture microstructure of the longitudinal cross-section of the as-cast LM24/SiC$_{np}$ composite subjected to the tensile test. In addition to the cracked Fe-bearing and Cu-bearing intermetallic compounds (Fig. 14a), the region where SiC nanoparticles were agglomerated was an additional site for crack initiation, due to the ease of debonding between SiC nanoparticles and Al matrix, as shown in Fig. 14b. Moreover, the areas containing mixed SiC agglomerations and Fe-bearing and/or Cu-bearing intermetallic phase, as indicated in Fig. 14c and d, could add to the vulnerable sites for
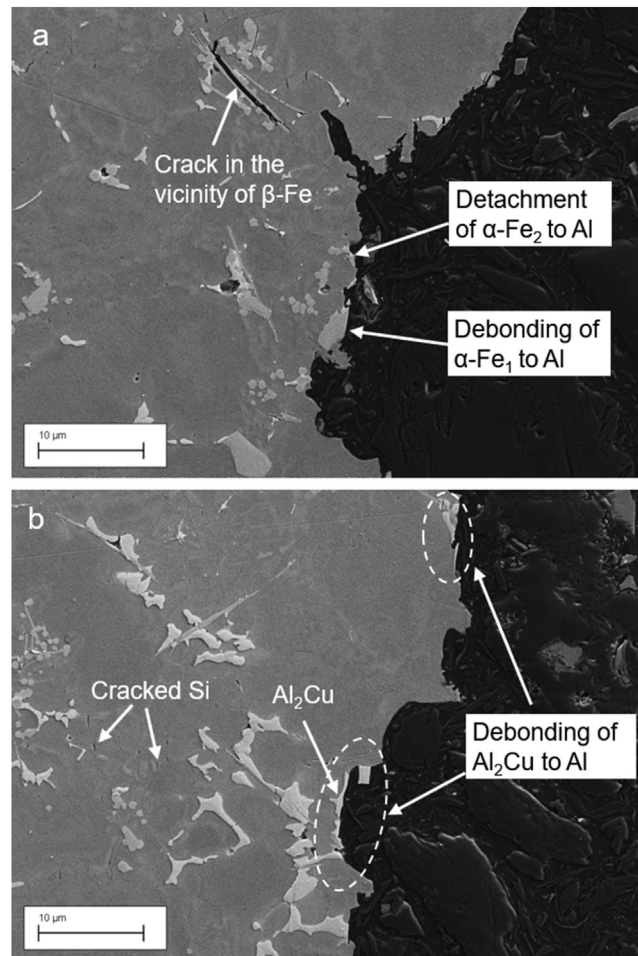
crack initiation and propagation. This could be detrimental to the ductility of the composites.

4. Discussion

4.1. Distribution of SiC nanoparticles and their effect on grain refinement

A relatively even distribution of loose SiC agglomerates, mainly located in the interdendritic or eutectic regions, was achieved, as shown in Fig. 7, suggesting that the combined physical pre-mixing and ultrasonic processing is a good practice. The existence of agglomerates in the interdendritic region indicated that the majority of SiC nanoparticles were pushed rather than engulfed by the solidification front (solid−liquid interface). When the molten aluminium containing dispersed SiC nanoparticles solidified, the interaction between the solidification front and nanoparticles occurred, resulting in re-distribution of the particles. In theory, the SiC nanoparticles could be either engulfed by the solidification front and consequently distributed in the interior of the grain,
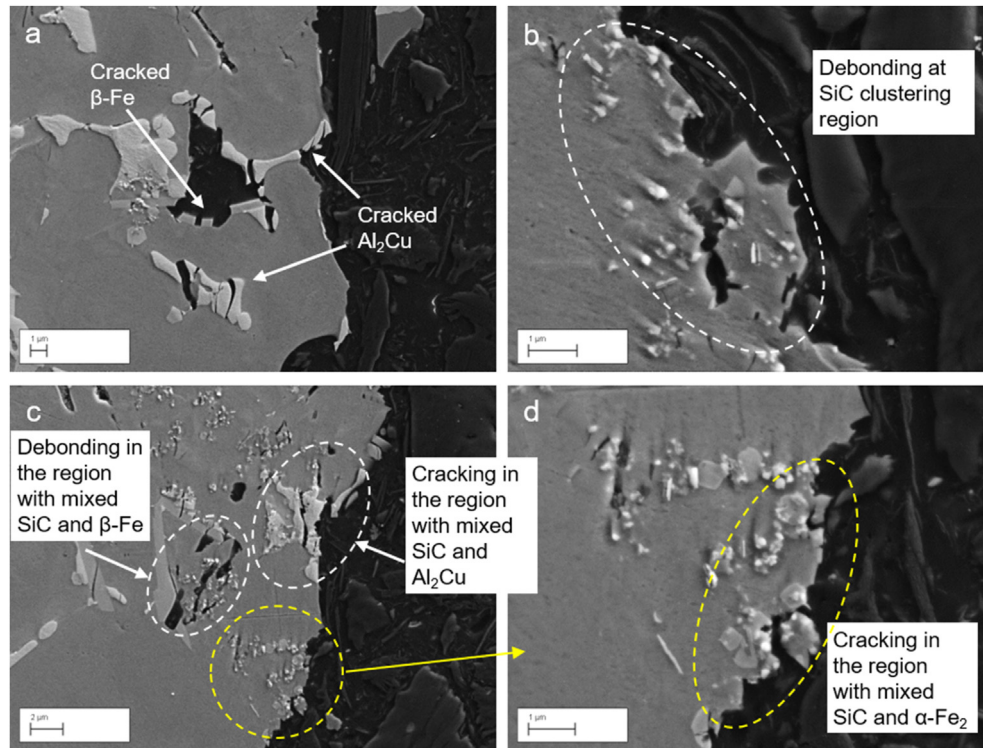
Fig. 14 — SE—SEM micrographs showing the crack structure on the longitudinal cross-section of as-cast LM24/SiC$_{np}$ composites subjected to the tensile test.

or pushed by the solid—liquid interface toward the grain boundaries. For a given particle size, it has been suggested [56,57] that a critical velocity of the solidification front can be calculated to push the particles by the solid—liquid interface, which is the solidification velocity above which particles are engulfed by the interface and below which they are pushed.

Whether particle expulsion or engulfment occurs is an extremely complicated phenomenon. Generally, the repulsive force from van der Waals potential and the dragging force originating from the flow of liquid are considered the two main parameters that determine the critical velocity for a specific particle in a given melt, on the basis of the assumptions that there is no adhesion of extra fluid or gas film on the nanoparticle and no chemical reaction between the nanoparticle and the melt. The gravity and buoyancy forces can be neglected since these forces are much smaller than the van der Waals force and dragging force [58]. The repulsive force and the dragging force compete with each other. If the repulsive force outstrips the dragging force, particles will be pushed, conversely, particles will be engulfed. The critical velocity, v_{cr}, can be calculated by the following equation [59]:

$$v_{cr} = \frac{A_{sys} \, (D_{cr} - 2D_s)}{36\pi R \eta D_{cr}^{\,2}} \qquad (1)$$

where, A_{sys} is the system Hamaker constant [60] of the LM24 melt-SiC particle system. D_{cr} represents the critical distance between the solidification front and the particle, at which the critical velocity is attained. D_s is approximately the diameter of a liquid molecule. R is the radius of the particle. η is the viscosity of the bulk liquid. Due to a lack of data on the

Hamaker constants and the viscosity of the LM24 liquid, A_{sys} and η for the liquid aluminium are used for estimation instead. The parameters can be obtained from Refs [59,61]: $A_{sys} = -1.09 \times 10^{-21}$ J, $\eta = 1$ mPa s, $D_{cr} = 1.2$ nm, $D_s = 03$ nm R is in the range of 10—50 nm in our case. Substituting these values into Eq. (1), v_{cr} is calculated to be 80—402 µm s^{-1}. The estimated v_{cr} is relatively large, particularly given the fact that the normal permanent mould casting can produce a solidification front velocity of the order of 1 µm s^{-1} [59]. It is noted from Eq. (1) that the critical velocity is increased with a decrease in particle size. In this sense, a higher cooling rate is therefore desired to obtain the engulfment of particles to cause a more homogeneous distribution of reinforcement.

In this study, the engulfment of the majority of the SiC nanoparticles was not achieved, despite very high cooling rates (10^3 K s^{-1} [62]) in the HPDC process. The solidification velocity in our case can be calculated by [63]:

$$v = \frac{d_{avg}}{8t_s} \qquad (2)$$

where, d_{avg} is the mean grain diameter size and t_s is the local solidification time. Taking the experimental d_{avg} as 15 µm and the t_s as 0.05 s, we have $v = 40$ µm s^{-1}. Ji et al. [64] has estimated the solidification velocity of an α-Al grain to be 3.9 µm s^{-1} in AlMgSi HPDC samples having the same dimensions as this study. This demonstrates that the local solidification velocity is considerably lower than the critical velocity, resulting in the pushing of the majority of the particles. However, the fine grain structure generated by HPDC improved the distribution of the nanoparticle clusters. The

pushed SiC nanoparticles or agglomerates could also restrict the grain growth due to the following facts: (1) the lower thermal conductivity of a SiC particle increased the temperature gradient ahead of the solidification front and therefore acted as a barrier to the removal of the heat necessary for further solidification; and (2) a SiC particle served as a barrier preventing solute diffusion away from the tip of the growing Al dendrite, thereby changing the concentration gradient and restricting growth. The present work demonstrating a nearly 40% decrease in the Al grain size, from ~24 ± 6 μm to ~15 ± 5 μm, indicating a significant grain growth restriction effect. The enhancement of the nucleation effect by the reinforced nanoparticles could be the potential reason for the grain refinement, but this was not investigated in the present study and is therefore not further discussed.

4.2. Strengthening mechanism

The mechanical test results showed that both the as-cast hardness and YS were improved by ~8%, after the 1wt% addition of SiC nanoparticles. This can be ascribed to the combined effects of the reduced Al grain size and CTE mismatch between SiC particles and the Al matrix. Compared to the as-cast properties, the yield strength after a T6 heat treatment was significantly increased by ~115% and ~102% for the LM24 and LM24/SiC$_{np}$ composite, respectively, which was primarily attributed to the precipitate strengthening by the β″ and θ′ phases, as indicated by the TEM observations (Figs. 8—10).

Since SiC particles and the Al matrix have different coefficients of thermal expansion (CTE), a large number of dislocations (Fig. 8b) can be generated during the cooling of the composite melt in the solidification process, due to the thermal mismatch between Al matrix and SiC particles/clusters and to accommodate the inconsistency of geometry variations. This caused a high work hardening rate and an enhanced strengthening effect. The increase in yield strength due to CTE difference can be expressed by the following equation [65]:

$$\Delta\sigma_{Dis} = A \cdot G \cdot \sqrt{\frac{\Delta a \cdot \Delta T \cdot V \cdot b}{2R}} \qquad (3)$$

where $A = 1.25$ is the geometric constant, $G = 26.2$ GPa is the shear module of aluminium, Δa is the difference of CTE between SiC (4×10^{-6} K^{-1}) and the Al matrix (23.8×10^{-6} K^{-1}), ΔT is the difference between the solidus temperature (793 K [66]) and testing temperature (298 K), V is the volume fraction of the SiC particles, which is deduced to be ~0.8 vol.% based on the 1 wt% addition, b is the Burgers vectors of the aluminium matrix which is 0.286 nm, and R is regarded as the radius of the individual or clusters of SiC particles, where R can be taken as 50—500 nm in this work due to the agglomerations. Based on these values, the $\Delta\sigma_{Dis}$ is calculated to be 4.6—14.7 MPa.

In contrast to the elevated strength observed, the slight decrease (from 3.6% to 3.3%) in elongation after the 1 wt% addition of SiC nanoparticles was attributed to the increased porosity (Fig. 3) and the additional "crack-prone" sites containing mixed agglomerates of SiC particles and intermetallic phases which formed during solidification, as shown in the fracture micrographs in Fig. 14.

Significantly, the precipitation strengthening was the dominant strengthening mechanism for the LM24 alloy and LM24/SiC$_{np}$ composite subjected to the T6 heat treatment. The β″ and θ′ phase were identified in both samples. These precipitate phases served as the main strengthening phases to retard dislocation gliding, interacting with dislocations through the Orowan strengthening mechanism, thereby delivering a considerably higher YS and UTS of 370 ± 7 MPa and 468 ± 12 MPa, respectively, compared to the previously reported AlSi9Cu3 HPDC alloy under a similar heat treatment [50], which delivered a YS of ~356 MPa and a UTS of ~431 MPa.

5. Conclusions

This work produced an LM24/SiC$_{np}$ composite by combining the advantages of stir mixing, ultrasonic treatment, and HPDC technology which generates a high solidification rate, in an attempt to explore the effect of incorporated SiC nanoparticles on the microstructure and mechanical properties of the LM24 alloy. From this study the following conclusions can thus be drawn:

- A relatively homogeneous distribution of loose SiC clusters was obtained in the LM24/SiC$_{np}$ composite, resulting from ultrasonic processing of melt and the fine grain structure caused by high cooling rates in the HPDC process. The SiC nanoparticles tended to distribute in the interdendritic regions because particles are pushed rather than engulfed by the solidification front despite the high cooling rate of the HPDC casting route which delivered solidification velocities lower than the estimated critical velocity of 80—402 μm s^{-1} that is needed for the SiC nanoparticle to be encapsulated.
- α-Al grains were effectively refined, with the grain size 24 ± 6 μm in the LM24 alloy, decreasing to 15 ± 5 μm in the composite. This was attributed to the grain growth restriction effect by pushed SiC nanoparticles which hindered or delayed the heat removal and solutal diffusion in the solidification front.
- Both the hardness and YS were improved by ~8%, after the addition of SiC nanoparticles, demonstrating a higher YS of ~187 MPa and a UTS of ~350 MPa in the as-cast LM24/SiC$_{np}$ composite, due to the effect of reduced α-Al grain size and CTE difference between the SiC and Al matrix.
- Both LM24 and LM24/SiC$_{np}$ displayed a significant increase in the strength after T6 heat treatment, with the YS increasing by 100—115%, which was mainly ascribed to the strengthening effect of the β″ and θ′ precipitates. Compared to commercially used AlSi9Cu3 HPDC alloys, the developed T6 heat-treated AlSi9Cu3-1wt%SiC$_{np}$ composite provided a significantly higher YS and UTS of ~370 MPa and ~468 MPa, respectively.

Credit authorship contribution statement

Guangyu Liu: Conceptualisation, Methodology, Data curation, Formal analysis, Investigation, Writing — original draft, review & editing.

Mahfuz Karim: Experiments, Investigation, Data curation, Formal analysis.

Shihao Wang: Investigation, TEM.

Dmitry Eskin: Conceptualisation, Writing − review & editing, Validation, Supervision.

Brian McKay: Funding acquisition, Conceptualisation, Writing − review & editing, Validation, Supervision.

Declaration of Competing Interest

The authors declare that they have no known competing financial interests or personal relationships that could have appeared to influence the work reported in this paper.

Acknowledgement

REFERENCES

[1] Ramnath BV, Elanchezhian C, Annamalai RM, Aravind S, Atreya TS, Vignesh V, et al. Aluminium metal matrix composites-a review. Rev Adv Mater Sci 2014;38(5):55–60.

[2] Chawla NC, Chawla KK. Metal-matrix composites in ground transportation. J Occup Med 2006;58(11):67–70.

[3] Miracle DB. Metal matrix composites—from science to technological significance. Compos Sci Technol 2005;65(15−16):2526–40.

[4] Alaneme KK, Sanusi KO. Microstructural characteristics, mechanical and wear behaviour of aluminium matrix hybrid composites reinforced with alumina, rice husk ash and graphite. Eng Sci Technol Int J 2015;18(3):416–22.

[5] Sadoun AM, Mohammed MM, Fathy A, El-Kady OA. Effect of Al_2O_3 addition on hardness and wear behavior of Cu−Al_2O_3 electro-less coated Ag nanocomposite. J Mater Res Technol 2020;9(3):5024–33.

[6] Sadoun AM, Mohammed MM, Elsayed EM, Meselhy AF, El-Kady OA. Effect of nano Al_2O_3 coated Ag addition on the corrosion resistance and electrochemical behavior of Cu-Al_2O_3 nanocomposites. J Mater Res Technol 2020;9(3):4485–93.

[7] Sadoun AM, Najjar IM, Abd-Elwahed MS, Meselhy A. Experimental study on properties of Al−Al_2O_3 nanocomposite hybridized by graphene nanosheets. J Mater Res Technol 2020;9(6):14708–17.

[8] Barakat WS, Wagih A, Elkady OA, Abu-Oqail A, Fathy A, El-Nikhaily A. Effect of Al_2O_3 nanoparticles content and compaction temperature on properties of Al−Al_2O_3 coated Cu nanocomposites. Compos B Eng 2019;175:107140.

[9] Wagih A, Fathy A, Sebaey TA. Experimental investigation on the compressibility of Al/Al_2O_3 nanocomposites. Int J Mater Prod Technol 2016;52(3−4):312–32.

[10] Shin JH, Choi HJ, Bae DH. The structure and properties of 2024 aluminum composites reinforced with TiO_2 nanoparticles. Mater Sci Eng, A 2014;607:605–10.

[11] Dixit A, Kumar K. Optimization of mechanical properties of silica gel reinforced aluminium MMC by using Taguchi method. Mater Today Proc 2015;2(4−5):2359–566.

[12] Alizadeh A, Abdollahi A, Biukani H. Creep behavior and wear resistance of Al 5083 based hybrid composites reinforced with carbon nanotubes (CNTs) and boron carbide (B4C). J Alloys Compd 2015;650:783–93.

[13] Krasnowski M, Gierlotka S, Kulik T. TiC−Al composites with nanocrystalline matrix produced by consolidation of milled powders. Adv Powder Technol 2015;26(5):1269–72.

[14] Rahman MH, Al Rashed HM. Characterization of silicon carbide reinforced aluminum matrix composites. Procedia Eng 2014;90:103–9.

[15] Shaat M, Fathy A, Wagih A. Correlation between grain boundary evolution and mechanical properties of ultrafine-grained metals. Mech Mater 2020;143:103321.

[16] Sharma P, Sharma S, Khanduja D. Production and some properties of Si_3N_4 reinforced aluminium alloy composites. J Asian Ceram 2015;3(3):352–9.

[17] Abd-Elwahed MS, Ibrahim AF, Reda MM. Effects of ZrO_2 nanoparticle content on microstructure and wear behavior of titanium matrix composite. J Mater Res Technol 2020;9(4):8528–34.

[18] Jia L, Kondoh K, Imai H, Onishi M, Chen B, Li SF. Nano-scale AlN powders and AlN/Al composites by full and partial direct nitridation of aluminum in solid-state. J Alloys Compd 2015;629:184–7.

[19] Smith CA. Discontinuous reinforcements for metal-matrix composites. DWA Aluminium Composites 2001. ASTM handbook Vol 21 Composites.

[20] Mavhungu ST, Akinlabi ET, Onitiri MA, Varachia FM. Aluminum matrix composites for industrial use: advances and trends. Procedia Manuf 2017;7:178–82.

[21] Tjong SC, Mai YW. Processing-structure-property aspects of particulate-and whisker-reinforced titanium matrix composites. Compos Sci Technol 2008;68(3−4):583–601.

[22] Zhang Z, Chen DL. Consideration of Orowan strengthening effect in particulate-reinforced metal matrix nanocomposites: a model for predicting their yield strength. Scripta Mater 2006;54(7):1321–6.

[23] Srivastava N, Chaudhari GP. Strengthening in Al alloy nano composites fabricated by ultrasound assisted solidification technique. Mater Sci Eng, A 2016;651:241–7.

[24] Habibnejad-Korayem M, Mahmudi R, Poole WJ. Enhanced properties of Mg-based nano-composites reinforced with Al_2O_3 nano-particles. Mater Sci Eng, A 2005;19(1−2):198–203.

[25] Nguyen QB, Gupta M. Enhancing compressive response of AZ31B magnesium alloy using alumina nanoparticulates. Compos Sci Technol 2008;68(10−11):2185–92.

[26] Dieter GE. Mechanical metallurgy. 3rd ed. NY): McGraw-Hill; 1986. p. 212–20.

[27] Dai LH, Ling Z, Bai YL. Size-dependent inelastic behavior of particle-reinforced metal−matrix composites. Compos Sci Technol 2001;61(8):1057–63.

[28] Vogt R, Zhang Z, Li Y, Bonds M, Browning ND, Lavernia EJ, et al. The absence of thermal expansion mismatch strengthening in nanostructured metal−matrix composites. Scripta Mater 2009;61(11):1052–5.

[29] Brown LM, Stobbs WM. The work-hardening of copper-silica v. equilibrium plastic relaxation by secondary dislocations. Philos Mag 1976;34(3):351–72.

[30] Schultz BF, Ferguson JB, Rohatgi PK. Microstructure and hardness of Al_2O_3 nanoparticle reinforced Al−Mg composites fabricated by reactive wetting and stir mixing. Mater Sci Eng, A 2011;530:87–97.

[31] Ferguson JB, Sheykh-Jaberi F, Kim CS, Rohatgi PK, Cho K. On the strength and strain to failure in particle-reinforced magnesium metal-matrix nanocomposites (Mg MMNCs). Mater Sci Eng, A 2012;558:193–204.

[32] Sadoun AM, Meselhy AF, Deabs AW. Improved strength and ductility of friction stir tailor-welded blanks of base metal

AA2024 reinforced with interlayer strip of AA7075. Results Phys 2020;16:102911.

[33] Attar S, Nagaral M, Reddappa HN, Auradi V. A review on particulate reinforced aluminum metal matrix composites. J Emerg Technol Innov Res 2015;2(2):225—9.

[34] Sadoun AM, Wagih A, Fathy A, Essa AR. Effect of tool pin side area ratio on temperature distribution in friction stir welding. Results Phys 2019;15:102814.

[35] Ardakani MR, Khorsand S, Amirkhanlou S, Nayyeri MJ. Application of compocasting and cross accumulative roll bonding processes for manufacturing high-strength, highly uniform and ultra-fine structured Al/SiC$_p$ nanocomposite. Mater Sci Eng, A 2014;592:121—7.

[36] Naher S, Brabazon D, Looney L. Computational and experimental analysis of particulate distribution during Al—SiC MMC fabrication. Composites Part A Appl Sci Manuf 2007;38(3):719—29.

[37] Hashim J, Looney L, Hashmi MS. Metal matrix composites: production by the stir casting method. J Mater Process Technol 1999;92:1—7.

[38] Segurado J, Gonzalez C, Llorca J. A numerical investigation of the effect of particle clustering on the mechanical properties of composites. Acta Mater 2003;51(8):2355—69.

[39] Nair SV, Tien JK, Bates RC. SiC-reinforced aluminium metal matrix composites. Int Mater 1985;30(1):275—90.

[40] Lloyd DJ. Aspects of fracture in particulate reinforced metal matrix composites. Acta Metall Mater 1991;39(1):59—71.

[41] Cao G, Konishi H, Li X. Mechanical properties and microstructure of SiC-reinforced Mg-(2, 4) Al-1Si nanocomposites fabricated by ultrasonic cavitation based solidification processing. Mater Sci Eng, A 2008;486(1—2):357—62.

[42] Suslick KS, Didenko Y, Fang MM, Hyeon T, Kolbeck KJ, McNamara III WB, et al. Acoustic cavitation and its chemical consequences. Philosophical transactions of the royal society of london. Proc Math Phys Eng Sci 1999;357(1751):335—53.

[43] Eskin DG. Ultrasonic processing of molten and solidifying aluminium alloys: overview and outlook. Mater Sci Technol 2017;33(6):636—45.

[44] Priyadarshi A, Khavari M, Subroto T, Prentice P, Pericleous K, Eskin D, et al. Mechanisms of ultrasonic de-agglomeration of oxides through in-situ high-speed observations and acoustic measurements. Ultrason Sonochem 2021;79:105792.

[45] Eskin GI, Eskin DG. Ultrasonic treatment of light alloy melts. 2nd ed. CRC Press; 2015.

[46] Ji S, Yan F, Fan Z. Development of a high strength Al—Mg2Si—Mg—Zn based alloy for high pressure die casting. Mater Sci Eng, A 2015;626:165—74.

[47] Dandekar CR, Shin YC. Modeling of machining of composite materials: a review. Int J Mach Tool Manufact 2012;57:102—21.

[48] Li Q, Rottmair CA, Singer RF. CNT reinforced light metal composites produced by melt stirring and by high pressure die casting. Compos Sci Technol 2010;70(16):2242—7.

[49] Hu Q, Zhao H, Li F. Microstructures and properties of SiC particles reinforced aluminum-matrix composites fabricated by vacuum-assisted high pressure die casting. Mater Sci Eng, A 2017;680:270—7.

[50] Lumley RN, O'Donnell RG, Gunasegaram DR, Givord M. Heat treatment of high-pressure die castings. Metall Mater Trans A 2007;38(10):2564—74.

[51] Zhang Y, Wang S, Lordan E, Wang Y, Fan Z. Improve mechanical properties of high pressure die cast Al9Si3Cu alloy via dislocation enhanced precipitation. J Alloys Compd 2019;785:1015—22.

[52] Belov NA, Eskin DG, Aksenov AA. Multicomponent phase diagrams: applications for commercial aluminum alloys. Elsevier; 2005.

[53] Xiao Q, Liu H, Yi D, Yin D, Chen Y, Zhang Y, et al. Effect of Cu content on precipitation and age-hardening behavior in Al-Mg-Si-xCu alloys. J Alloys Compd 2017;695:1005—13.

[54] Eskin DG. Decomposition of supersaturated solid solutions in Al—Cu—Mg—Si alloys. J Mater Sci 2003;38(2):279—90.

[55] Wang SC, Starink MJ. Precipitates and intermetallic phases in precipitation hardening Al—Cu—Mg—(Li) based alloys. Int Mater 2005;50(4):193—215.

[56] Sen S, Dhindaw BK, Stefanescu DM, Catalina A, Curreri PA. Melt convection effects on the critical velocity of particle engulfment. J Cryst Growth 1997;173(3—4):574—84.

[57] Youssef YM, Dashwood RJ, Lee PD. Effect of clustering on particle pushing and solidification behaviour in TiB$_2$ reinforced aluminium PMMCs. Composites Part A Appl Sci Manuf 2005;36(6):747—63.

[58] Ozsoy IB, Li G, Choi H, Zhao H. Shape effects on nanoparticle engulfment for metal matrix nanocomposites. J Cryst Growth 2015;422:62—8.

[59] Xu JQ, Chen LY, Choi H, Li XC. Theoretical study and pathways for nanoparticle capture during solidification of metal melt. J Phys Condens Matter 2012;24(25):255304.

[60] Hamaker HC. The London-van der Waals attraction between spherical particles. Physica 1937;4(10):1058—72.

[61] Dehghan Hamedan A, Shahmiri M. A new model for the solidification of metal matrix nanocomposites: wet cluster engulfment of nanoparticles by the solidification front. J Compos Mater 2017;51(20):2913—32.

[62] Zhu X, Dong X, Blake P, Ji S. Improvement in as-cast strength of high pressure die-cast Al—Si—Cu—Mg alloys by synergistic effect of Q-Al$_5$Cu$_2$Mg$_8$Si$_6$ and θ-Al$_2$Cu phases. Mater Sci Eng, A 2021;802:140612.

[63] Chen XH, Yan H. Solid—liquid interface dynamics during solidification of Al 7075—Al$_2$O$_{3np}$ based metal matrix composites. Mater Des 2016;94:148—58.

[64] Ji S, Wang Y, Watson D, Fan Z. Microstructural evolution and solidification behavior of Al-Mg-Si alloy in high-pressure die casting. Metall Mater Trans A 2013;44(7):3185—97.

[65] Tao R, Zhao Y, Kai X, Zhao Z, Ding R, Liang L, et al. Effects of hot rolling deformation on the microstructure and tensile properties of an in situ-generated ZrB$_2$ nanoparticle-reinforced AA6111 composite. Mater Sci Eng, A 2018;732:138—47.

[66] Zhou B, Kang Y, Qi M, Zhang H, Zhu G. R-HPDC process with forced convection mixing device for automotive part of A380 aluminum alloy. Materials 2014;7(4):3084—105.